CONDENSED MATTER PHYSICS

Spin homojunction with high interfacial transparency for efficient spin-charge conversion

Lei Han[1]†, Yuyan Wang[2]†, Wenxuan Zhu[1], Runni Zhao[3], Xianzhe Chen[1], Rongxuan Su[1], Yongjian Zhou[1], Hua Bai[1], Qian Wang[1], Yunfeng You[1], Chong Chen[1], Sen Yan[3], Tongjin Chen[1], Yongzheng Wen[3], Cheng Song[1]*, Feng Pan[1]*

High interfacial transparency is vital to achieve efficient spin-charge conversion for ideal spintronic devices with low energy consumption. However, in traditional ferromagnetic/nonmagnetic heterojunctions, the interfacial Rashba spin-orbit coupling brings about spin memory loss (SML) and two-magnon scattering (TMS), quenching spin current crossing the heterointerfaces. To address the intrinsic deficiency of heterointerface, we design a ferromagnetic FeRh/antiferromagnetic FeRh spin homojunction for efficient spin-charge conversion, verified by a high interfacial transparency of 0.75 and a high spin torque efficiency of 0.34 from spin pumping measurements. First-principles calculations demonstrate that the interfacial electric field of homojunction is two orders of magnitude smaller than that of traditional heterojunction, producing negligible interfacial spin-orbit coupling to drastically reduce SML and TMS. Our spin homojunction exhibits potential and enlightenment for future energy-efficient spintronic devices.

INTRODUCTION

Pursing efficient spin-charge conversion lies at the heart of spintronics (*1*, *2*). Numerous candidate materials for spin-charge conversion have emerged, such as heavy metals (*3*) and alloys (*4*–*6*), transition-metal dichalcogenides (*7*, *8*), transition-metal oxides (*9*), and antiferromagnets (*10*, *11*). Notably, the spin transmission through the interface between the spin source layer and the spin sink layer is inevitably involved in all the spin-charge conversion process, such as the spin Hall effect and the inverse spin Hall effect (ISHE) (*12*), spin-orbit torques (*13*), and the spin Hall magnetoresistance (*14*). Nevertheless, because of the existence of large interfacial spin-orbit coupling (*15*–*17*), spin memory loss (SML) (*18*–*20*) and two-magnon scattering (TMS) (*21*, *22*) greatly reduce the interfacial transparency (*23*–*25*). On one hand, low interfacial transparency attenuates the spin-charge conversion efficiency drastically, although the spin source and the spin sink material may have strong spin-charge conversion capabilities. On the other hand, the ignorance of interfacial transparency results in an unphysical overestimation of effective spin mixing conductance $G_{\mathrm{eff}}^{\uparrow\downarrow}$ (*22*). This leads to inaccurate estimations of the spin Hall angle θ_{SH} and the spin diffusion length λ_s, which scatters in a large scale, such as θ_{SH} (0.004 to 0.64) and λ_s (0.5 to 10 nm) for the commonly used material Pt (*22*, *26*). Therefore, improving the interfacial transparency is not only critical to efficient spin-charge conversion but also of great physical significance to the accurate determination of transport parameters and explanation of spin physics.

Interface engineering has been used to improve the interfacial transparency, including interfacial alloying (*27*) or inserting layers such as metal Hf (*28*), Cu (*29*, *30*), and insulator NiO (*31*). However, these methods introduce new spin carriers (magnons) and new interfaces, complicating both film preparation and physical understanding. If the spin source and the spin sink are different materials to construct a "spin heterojunction" (Fig. 1A) with broken inversion symmetry, the interfacial spin-orbit coupling can be hardly eliminated. An ideal solution is an epitaxial "spin homojunction" with similar crystal structures and elemental composition for the spin source and the spin sink (Fig. 1B). It is reasonable to expect that the interfacial electric field can also be substantially weakened because of the conserved inversion symmetry, resulting in negligible interfacial Rashba spin-orbit coupling (*15*) and concomitant low SML and TMS. On the basis of this design, a spin homojunction with high interfacial transparency for efficient spin-charge conversion is promising but remains elusive.

Iron-rhodium alloy (FeRh) is an intriguing spintronic material having first-order phase transition between antiferromagnetic (AFM) and ferromagnetic (FM) when sweeping temperature, potentially used in heat-assisted magnetic recording and magnetic refrigerant (*32*–*34*). Recently, the spin pumping effect was verified in FM-FeRh/Pt and NiFe/AFM-FeRh films with a high $\theta_{\mathrm{SH}}\lambda_s$ value of ~0.2 to 0.8 for FeRh (*35*). The high $\theta_{\mathrm{SH}}\lambda_s$ value indicates a superior intrinsic spin-charge conversion capability of FeRh alloy (*19*, *26*, *35*, *36*). Meanwhile, the FM and the AFM phase of the same FeRh material can separately play the role of the spin source layer and the spin sink layer, which brings about possibilities for a FeRh-based homojunction. Here, we design an FM-FeRh/AFM-FeRh spin homojunction for efficient spin-charge conversion, demonstrated by spin pumping measurements. The interfacial transparency T reaches 0.75 and the spin torque efficiency ξ_{DL}^{j} is up to 0.34, which are higher than traditional heavy metal/FM spin heterojunctions based on the spin Hall effect, such as Pt/Py (*22*, *24*). First-principles calculations reveal that the interfacial Rashba spin-orbit coupling of this FM-FeRh/AFM-FeRh

[1]Key Laboratory of Advanced Materials (MOE), School of Materials Science and Engineering, Tsinghua University, Beijing 100084, P. R. China. [2]Beijing National Research Center for Information Science and Technology, Tsinghua University, Beijing 100084, P. R. China. [3]State Key Laboratory of New Ceramics and Fine Processing, School of Materials Science and Engineering, Tsinghua University, Beijing 100084, P. R. China.
*Corresponding author. Email: songcheng@mail.tsinghua.edu.cn (C.S.); panf@mail.tsinghua.edu.cn (F.P.)
†These authors contributed equally to this work.

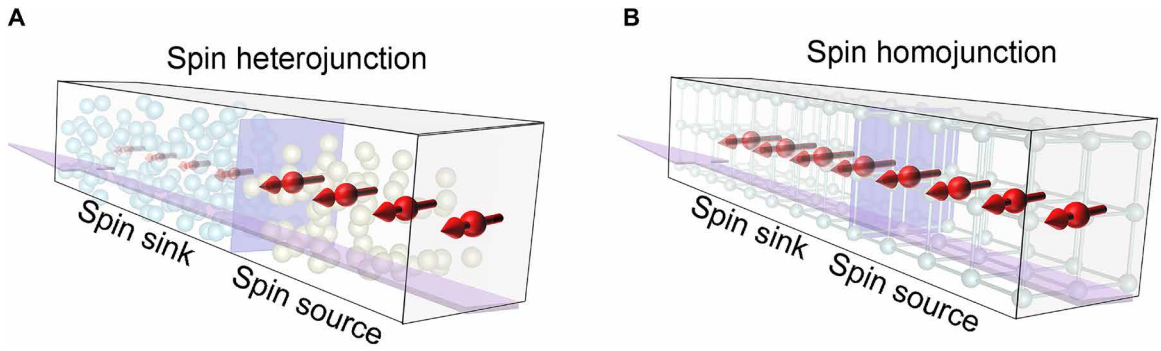

Fig. 1. Schematic of spin heterojunction and spin homojunction for spin transmission. (**A**) Spin heterojunction. (**B**) Spin homojunction.

spin homojunction is negligibly small, highly suppressing the SML and the TMS. Novel spin homojunction brings about a new dimension to the pursuit of efficient spin-charge conversion.

RESULTS

Growth and characterizations of the spin homojunction

We prepared 15-nm FeRh films on MgO(001) substrates by magnetron sputtering under different Ar pressures at 300°C, followed by annealing at 750°C for 1 hour. Figure 2A shows the temperature-dependent four-point resistivity (ρ-*T*) curves of the FeRh film grown at the Ar pressure of 0.4 and 0.7 Pa, with an in-plane (IP) field of 5 T. Abrupt decrease/increase of resistivity is observed when the temperature increases/decreases, corresponding to the AFM-FM and FM-AFM phase transition, respectively (*32*, *33*). As the Ar pressure increases from 0.4 to 0.7 Pa, the composition of FeRh changes from $Fe_{0.52}Rh_{0.48}$ to $Fe_{0.50}Rh_{0.50}$, making the room-temperature (RT) phase of FeRh change from FM to AFM, denoted as FM-FeRh and AFM-FeRh, respectively. Figure 2B presents the x-ray diffraction (XRD) spectra of these FM-FeRh and AFM-FeRh films. They exhibit strong FeRh(001) texture with diffraction peaks located at similar diffraction angles, indicating highly matched lattice constants. The average roughness (R_a) of 15-nm-thick FM-FeRh and AFM-FeRh films is 0.15 and 0.25 nm, respectively, showing a flat surface (fig. S1). As a result, different magnetic phases at RT, highly matched lattice and composition, as well as flat surfaces of FM-FeRh and AFM-FeRh single layers provide perquisite for a high-equality spin homojunction of FM-FeRh/AFM-FeRh.

Next, the FM-FeRh (15 nm)/AFM-FeRh (12 nm) homojunction is prepared by in situ tuning of Ar pressure from 0.4 to 0.7 Pa during sputtering of the FM-FeRh layer, followed by the AFM-FeRh layer. As shown in Fig. 2C, there are two hysteresis windows in the ρ-*T* loop of the homojunction, originated from two phase transitions of FM-FeRh and AFM-FeRh layers. XRD spectra at high diffraction angles are displayed in Fig. 2D, corresponding to the diffraction peaks of FeRh(300) for the FM-FeRh, the AFM-FeRh, and the FM-FeRh/AFM-FeRh homojunction. The diffraction angle of AFM-FeRh is slightly larger than that of FM-FeRh, consistent with the compressive stress in AFM-FeRh to stabilize the AFM phase (*37*). Notably, the XRD spectrum of FM-FeRh/AFM-FeRh exhibits two diffraction peaks, as a combination of both layers. To make in-depth characterization of the homointerface of our homojunction, we

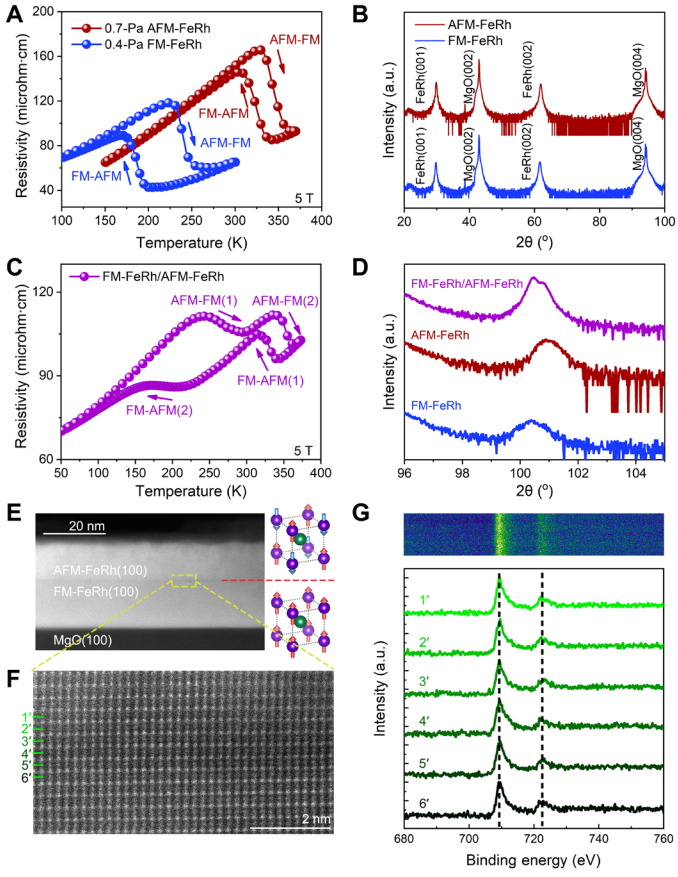

Fig. 2. Characterization of the FM-FeRh/AFM-FeRh spin homojunction. (**A**) ρ-*T* curves of individual FM-FeRh and AFM-FeRh thin films under an IP magnetic field of 5 T. (**B**) XRD spectra of the FM-FeRh and the AFM-FeRh thin films. a.u., arbitrary units. (**C**) ρ-*T* curve of the FM-FeRh/AFM-FeRh homojunction under an IP magnetic field of 5 T. (**D**) XRD spectra of the FM-FeRh, the AFM-FeRh, and the FM-FeRh/AFM-FeRh homojunction at high diffraction angle. (**E**) HAADF-STEM image of the FM-FeRh/AFM-FeRh homojunction. The red dash line indicates the interface between the FM-FeRh layer and the AFM-FeRh layer. Schematics of crystalline layout are included, where the purple and green atoms represent Fe and Rh atoms, and the vectors indicate the direction of spin. (**F**) High-resolution HAADF-STEM image and corresponding (**G**) EELS spectrum of the FM-FeRh/AFM-FeRh homojunction at the interface. Fe L_{2-3} edge fine structures are extracted from 1′ to 6′ Fe atomic planes.

performed the cross-sectional high-angle annular dark-field scanning transmission electron microscopy (HAADF-STEM). The interface between the FM-FeRh and the AFM-FeRh can be observed in Fig. 2E, as denoted by a red dash line. The contrast of the interface is low, indicating similar structure and composition of the FM-FeRh bottom layer and the AFM-FeRh upper layer. Figure 2F displays a high-resolution HAADF-STEM cross-sectional image of the FM-FeRh/AFM-FeRh interface with few interfacial disorders, where the electron energy-loss spectroscopy (EELS) spectra in Fig. 2G are acquired. Brighter Rh atoms are located at the body center of darker Fe atoms, indicating bcc α′-FeRh phase for both FM-FeRh and AFM-FeRh, which is able to exhibit the phase transition characteristic (*32*). Concomitant schematics of crystalline layout are displayed in Fig. 2E. The full epitaxial growth relationship with substrate is determined to be MgO(001)[010]//α′-FM-FeRh(001)[110]//α′-AFM-FeRh(001)[110] by φ-scan XRD measurements (fig. S2), highly consistent with the HAADF-STEM image. As indicated by the Fe L_{2-3} edge fine structures extracted from 1′ to 6′ atomic planes of Fe (Fig. 2G), the binding energy of Fe does not change when crossing the interface of FM-FeRh and AFM-FeRh, demonstrating analogous valence states of Fe atoms in the FM-FeRh layer and the AFM-FeRh layer. Therefore, the spin homojunction is composed of FM-FeRh and AFM-FeRh with distinct FM and AFM magnetic phases while with similar crystal structure and chemical environment for the spin source and the spin sink.

Spin pumping measurements for the spin homojunction

Spin pumping measurements were carried out to investigate the spin-charge conversion efficiency of the FM-FeRh/AFM-FeRh homojunction. As shown in Fig. 3A, spin pumping process involves spin current generated by microwave-excited FM resonance (FMR) of the FM-FeRh layer, transmitted through the homointerface of FM-FeRh/AFM-FeRh and converted to charge current via the ISHE in the AFM-FeRh layer (*38*). Details for device configurations and measurement principles are discussed in Materials and Methods. Figure 3B presents a typical voltage signal of the stripe along FM-FeRh/AFM-FeRh[110] when sweeping the magnetic field along the direction with the out-of-plane (OOP) polar angle θ_H of 90° and the IP azimuthal angle φ_H of 45°, under the excitation of 17-GHz, 19-dBm microwave. The resonance curve can be divided into symmetric and antisymmetric Lorentz line shapes as $V = V_{asym}L_{asym} + V_{sym}L_{sym}$, drawn by yellow and blue lines. $L_{asym} = -4\Delta H(H - H_R)/[4(H - H_R)^2 + \Delta H^2]$ and $L_{sym} = \Delta H^2/[4(H - H_R)^2 + \Delta H^2]$, where ΔH and H_R are the linewidth and the resonance field, respectively. anisotropic magnetoresistance (AMR) contributes to both symmetric and antisymmetric line shapes, while ISHE only contributes to symmetric line shape. The AMR component is zero at $\varphi_H = 0°$, 90°, 180°, and 270°, while the ISHE signal theoretically disappears only at $\varphi_H = 0°$ and 180° (*35*, *39*). Hence, as shown in Fig. 3C, spin pumping measurements at $\varphi_H = 90°$ and 270° reveal opposite pure ISHE signals with symmetric line shape, well matching the ISHE effect. For the stripe along FM-FeRh/AFM-FeRh[100], the spin pumping signal is slightly smaller (fig. S3). We focus on the stripes along FM-FeRh/AFM-FeRh[110] in the following measurements. Note that the actual microwave power on the stripe is measured to be 7.5 dBm because of microwave loss by a thermal-equivalent method (fig. S4). A clear linear dependence of signals with microwave power confirms that we are still in the linear regime of excitation (fig. S5).

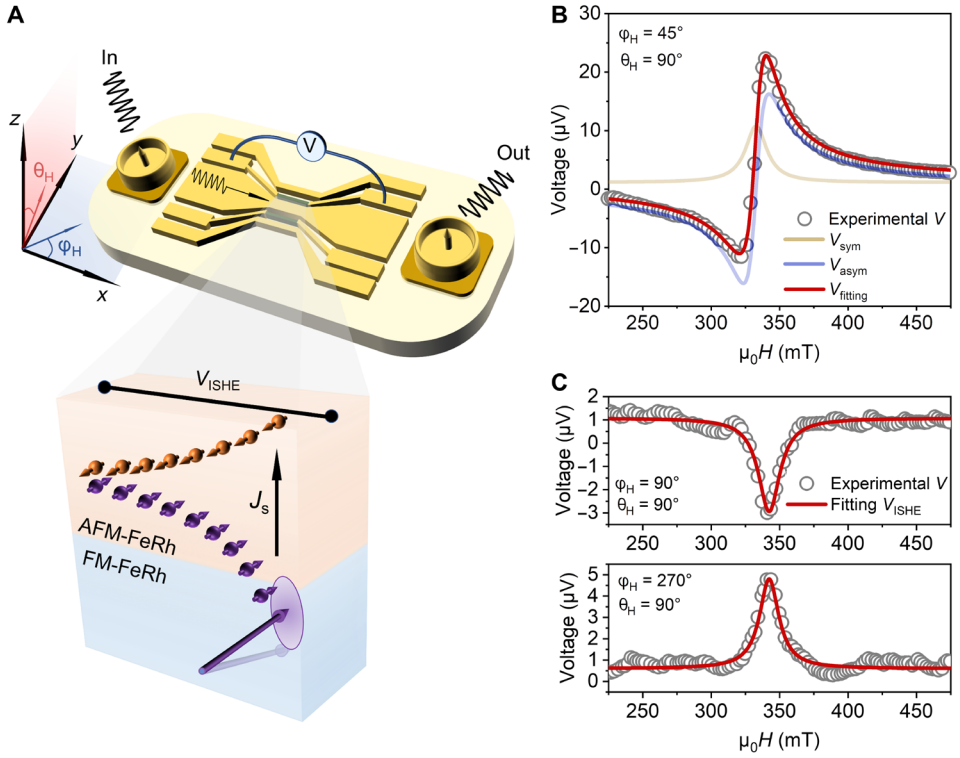

Fig. 3. Spin pumping measurements for the FM-FeRh/AFM-FeRh spin homojunction. (**A**) Schematic of the spin pumping experimental setup and principles. (**B**) Typical resonance curve measured at $\theta_H = 90°$ and $\varphi_H = 45°$ excited by the microwave of 17 GHz, 19 dBm. (**C**) Symmetric resonance signals from pure ISHE at $\varphi_H = 90°$ and $\varphi_H = 270°$, equivalent to reversing the polarity of the magnetic field.

Thermal effects usually have negligible contribution to spin pumping signals, especially under such a low microwave power (*40*–*42*).

Angle-dependent measurements were performed to demonstrate the spin pumping process with the exclusion of AMR signals more specifically. The magnetic field is swept at different φ_H, and corresponding symmetric and antisymmetric parts of signals at each φ_H are extracted to draw Fig. 4 (A and B, respectively). Note that inductive currents in the AFM-FeRh layer can also give a *y*-oriented Oersted field $\boldsymbol{h}_{IP}$ to excite the adjacent FM-FeRh, in addition to the $\boldsymbol{h}_{OOP}$ excitation field from the microwave in the coplanar waveguide (CPW). Thus, AMR and ISHE signals are originated from both IP and OOP excitation source. We fit the angle-dependent curve by the following expressions (detailed derivations can be found in Materials and Methods)

$$V_{asym} = U_{AMR}^{IP,asym} + U_{AMR}^{OOP,asym} = A\cos^2\varphi_M\sin\varphi_M + B\sin2\varphi_M$$

$$V_{sym} = U_{ISHE}^{OOP,sym} + (U_{AMR}^{IP,sym} + U_{ISHE}^{IP,sym}) + U_{AMR}^{OOP,sym} = C\sin\varphi_M + D\cos^2\varphi_M\sin\varphi_M + E\sin2\varphi_M \quad (1)$$

where φ_M is the azimuthal angle from *x* axis to the magnetization direction, which is approximately equal to φ_H here because the excitation frequency and the resultant resonance field are quite high. From the fitting, we obtain $C = -3.9$ μV, which is consistent with the magnitude of the spin pumping voltage observed at 90° and 270° (Fig. 3C). No exchange bias is found in our homojunction (fig. S6), judged by the *M*-*H* curve and the angle-dependent resonance field data (*43*). Consequently, angle-dependent experiments further verify the spin pumping process from FM-FeRh to AFM-FeRh in the FM-FeRh/AFM-FeRh spin homojunction.

Frequency-dependent measurements were carried out to investigate the spin transmission properties of the homogenous interface between FM-FeRh and AFM-FeRh, quantified by the effective spin mixing conductance $G_{eff}^{\uparrow\downarrow}$. Figure 4C shows the dispersion relation of the resonance frequency *f* versus the resonance field $\mu_0 H_R$ at $\varphi_H = 45°$. We use the simplified Kittel formula $f = \frac{\gamma\mu_0}{2\pi}\sqrt{H(H + M_{eff})}$ [considering $\varphi_M = \varphi_H$ due to the negligible anisotropy of FM-FeRh (fig. S6)] to fit and get the effective magnetization $\mu_0 M_{eff} = 863.59$ mT, along with the gyromagnetic ratio $\gamma = 176.22$ GHz T^{-1}. The saturation magnetization $\mu_0 M_s$ is measured to be 926.29 mT. Figure 4D presents the linear growth of resonance linewidth ΔH with *f*, which can be described by (*35*)

$$\mu_0\Delta H = \mu_0\Delta H_0 + 2\alpha_{FM/AFM}\frac{2\pi f}{\gamma} \quad (2)$$

where $\mu_0\Delta H_0$ is the inhomogeneous term, which is independent with *f*. $\alpha_{FM/AFM}$ is the effective damping of the FM-FeRh/AFM-FeRh

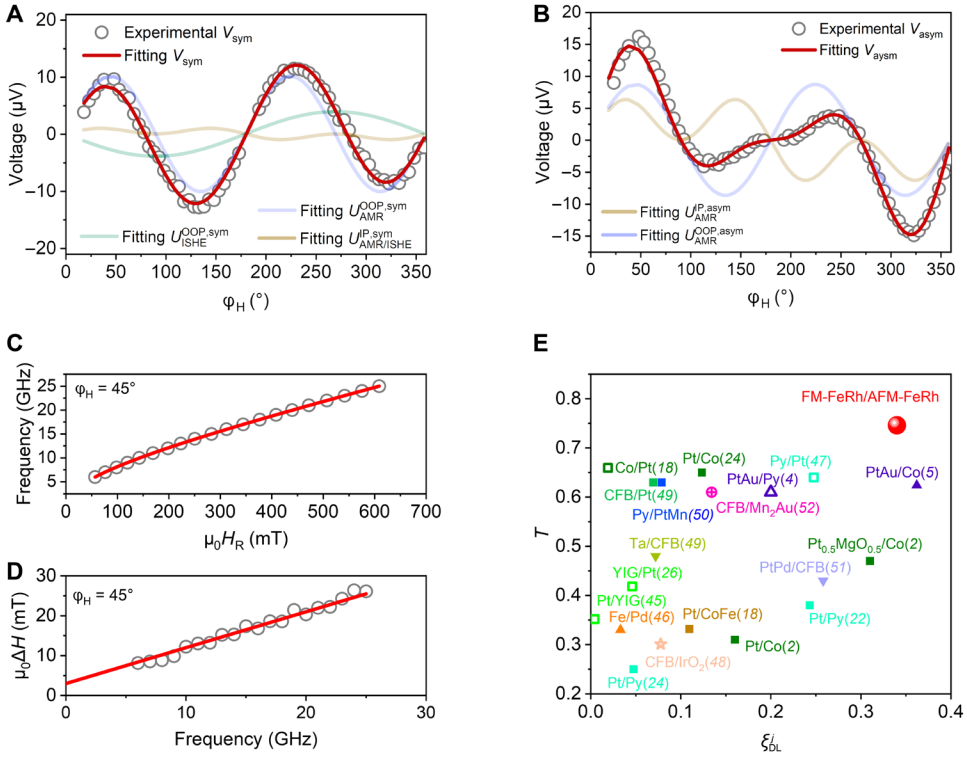

Fig. 4. Frequency-dependent and angle-dependent spin pumping measurements for the FM-FeRh/AFM-FeRh spin homojunction. (**A**) Symmetric and (**B**) asymmetric angle-dependent line shapes measured at 17 GHz, 19 dBm. (**C**) The resonance frequency *f* as a function of the resonance magnetic field H_R at $\varphi_H = 45°$. (**D**) The relationship between the resonance linewidth ΔH and the resonance frequency *f* at $\varphi_H = 45°$. (**E**) Comparison of the interfacial transparency *T* and the spin torque efficiency ξ_{DL}^{j} of our spin homojunction with representative works. Several topological materials and transition-metal dichalcogenides are also candidate spin sources but not included, because the former is beyond the scope of the spin Hall effect and the latter's interfacial transparency is seldom reported. The hollow points denote the results that are not directly presented in corresponding papers but are calculated by Eq. 5 according to relevant data given in corresponding papers. Solid points are given directly in corresponding papers. CFB denotes CoFeB and Py represents NiFe alloy.

homojunction. $\alpha_{FM/AFM}$ equals 0.0125 as fitted by Eq. 2. Then, $G_{eff}^{\uparrow\downarrow}$ of the interface of FeRh(AFM)/FeRh(FM) can be quantified by (*22*)

$$G_{eff}^{\uparrow\downarrow} = \frac{2M_s d_{FM} e^2}{\mu_B g \hbar}\Delta\alpha \quad (3)$$

where μ_B is the Bohr magnetron, g is the g factor, $\hbar$ is the reduced Planck constant, e is the electron charge, and d_{FM} is the thickness of FM-FeRh, respectively. $\Delta\alpha = \alpha_{FM/AFM} - \alpha_{FM}$. α_{FM} represents the damping of the FM-FeRh single layer, which is determined to be 0.0115 by Eq. 2 with frequency-dependent measurements under the same condition as FM-FeRh/AFM-FeRh (fig. S7). No observable resonant signals are found for an AFM-FeRh single layer (fig. S8). The $G_{eff}^{\uparrow\downarrow}$ is then calculated to be 0.259×10^{15} ohm^{-1} m^{-2}, corresponding to a $g_{eff}^{\uparrow\downarrow}$ of 6.69×10^{18} m^{-2}.

The interfacial transparency and the spin torque efficiency of the spin homojunction

The interfacial transparency T is related to the spin mixing conductance $G^{\uparrow\downarrow}$ of the FM-FeRh/AFM-FeRh interface according to the drift-diffusion model (*24*)

$$T = \frac{G^{\uparrow\downarrow}\tanh\left(\frac{d_{AFM}}{2\lambda_s}\right)}{G^{\uparrow\downarrow}\coth\left(\frac{d_{AFM}}{\lambda_s}\right) + \frac{G_{AFM}}{2}} \quad (4)$$

where λ_s and d_{AFM} are the spin diffusion length and the thickness of the AFM-FeRh. $G_{AFM} = 1/\lambda_s\rho_{AFM}$ denotes the spin conductance of the AFM-FeRh (*22*), and ρ_{AFM} is the resistivity of the AFM-FeRh, measured to be 144 microhm·cm. λ_s is measured to be around 1 nm (fig. S9), which is close to former works by FMR measurements ($\lambda_s < 1.15$ nm) (*33*). Considering $d_{AFM} >> \lambda_s$, $G^{\uparrow\downarrow} = \frac{G_{eff}^{\uparrow\downarrow} G_{AFM}}{G_{AFM} - 2G_{eff}^{\uparrow\downarrow}}$, and then T can be simplified as (*22*)

$$T = \frac{2G_{eff}^{\uparrow\downarrow}}{G_{AFM}} \sim 0.75 \quad (5)$$

To further investigate the spin-charge conversion efficiency of the FM-FeRh/AFM-FeRh homojunction, we calculate the spin Hall angle θ_{SH} of AFM-FeRh by $\theta_{SH} = \frac{V_{ISHE}\hbar}{2eRJ_s w\lambda_s \sin\varphi_M}$ (*35*), where V_{ISHE} is the inverse spin Hall voltage generated by the spin pumping process. R and w are the resistance and the width of stripe, equaling 1989 ohms and 6 μm, respectively. J_s is the magnitude of spin current at the interface. We carefully calibrate the microwave current by the thermal-equivalent method and calculate $\boldsymbol{h}_{OOP}$ via the electromagnetic field simulation with COMSOL Multiphysics (fig. S4), and then J_s can be determined. As a result, θ_{SH} is calculated as 0.46. Detailed deviations are included in Materials and Methods. After that, ξ_{DL}^j, which represents the damping-like spin Hall torque efficiency per unit current density (*2*), can be determined as

$$\xi_{DL}^j = T\theta_{SH} = 0.34 \quad (6)$$

We also carried out spin-torque FMR for independent verification, which is widely used to extract ξ_{DL}^j (*44*). ξ_{DL}^j turns out to be 0.28, consistent with the spin pumping measurements within experimental uncertainty (fig. S9 and table S1). Besides, the spin polarization direction of spin current from AFM-FeRh is found to be dependent on Néel vector (fig. S10). ξ_{DL}^j of a reference FM-FeRh(15 nm)/Pt(12 nm) heterojunction is measured to be 0.18, indicating the high spin-torque efficiency of our homojunction (fig. S11).

As presented in Fig. 4E, we compare T and ξ_{DL}^j of our FM-FeRh/AFM-FeRh homojunction with that of available and representative two-layer heterojunctions for spin-charge conversion, including heavy metals and alloys, transition-metal oxides, antiferromagnets, etc. (*2*, *4*, *5*, *22*, *24*, *26*, *45*–*52*). As a result, our FM-FeRh/AFM-FeRh spin homojunction has a high interfacial transparency T and a high ξ_{DL}^j, demonstrating its unique advantage for spin-charge conversion.

DISCUSSION

It should be noted that the damping enhancement $\Delta\alpha$ is usually not simply originated from the spin pumping effect (*2*, *18*, *19*, *22*). Specifically, considering SML and TMS, $\alpha_{FM/AFM}$ can be expressed as

$$\alpha_{FM/AFM} = \alpha_{Gil} + \alpha_{SML} + \alpha_{TMS} + \alpha_{SP} \quad (7)$$

where α_{Gil}, α_{SP}, α_{SML}, and α_{TMS} parameter the intrinsic Gilbert damping, the damping from SML, TMS, and the spin pumping effect. As a result

$$\Delta\alpha = \alpha_{FM/AFM} - \alpha_{FM} = \alpha_{FM/AFM} - \alpha_{Gil} = \alpha_{SML} + \alpha_{TMS} + \alpha_{SP} \quad (8)$$

It means that the ignorance of additional damping due to SML and TMS gives rise to an unphysically giant $G_{eff}^{\uparrow\downarrow} \propto \Delta\alpha$ and resultant overestimations of $T \propto G_{eff}^{\uparrow\downarrow}$ and $\xi_{DL}^j \propto G_{eff}^{\uparrow\downarrow}$ (*22*). Principally, the true $G_{eff}^{\uparrow\downarrow}$ has two upper limits (*22*): (i) $G_{eff}^{\uparrow\downarrow}$ should be at least less than $2G_{AFM}$; otherwise, a negative $G^{\uparrow\downarrow}$ will be obtained and T will excess 1 according to Eqs. 4 and 5. (ii) $G^{\uparrow\downarrow}$ has a limitation of $G^{\uparrow\downarrow} < G_{sh}$, where G_{sh} is the Sharvin conductance of the AFM-FeRh. Hence, $G_{eff}^{\uparrow\downarrow} < (G_{sh}G_{AFM})/(2G_{sh} + G_{AFM})$. The violation of the above two limitations indicate non-negligible SML or TMS at the interface (*53*–*55*), and these reports are not included in Fig. 4E.

Next, we theoretically investigate the influence of α_{SML} and α_{TMS} in our spin homojunction. (i) First, both SML and TMS have been demonstrated to be intrinsically determined by the magnitude of the interfacial Rashba spin-orbit coupling $V(\mathbf{r}) = \alpha_R\delta(z)(\hat{\boldsymbol{k}} \times \hat{\boldsymbol{z}})\cdot\boldsymbol{\sigma}$ (*15*, *16*, *20*–*22*). Here, α_R denotes the Rashba coefficient, which is proportional to the magnitude of the interfacial electric field (*56*). The interfacial electric field is calculated for both our FM-FeRh/AFM-FeRh homojunction and a common Fe/Pt heterojunction for comparison. Atomic spin-orbit coupling is included to consider the influence of magnetic symmetry breaking on the interfacial electric field. As shown in Fig. 5A, the evolution feature of charge density along the OOP z direction is quite similar before and after stepping crosshomogeneous interface (indicated by yellow shadow), and thus, the averaged planar potential in Fig. 5B only varies 0.04 eV. In contrast, the charge density changes severely between the heterogeneous interface of Pt and Fe, as presented in Fig. 5C. Hence, the averaged planar potential experiences a sharp increase of 7.71 eV from Pt to Fe (Fig. 5D), two orders of magnitude larger than that of the homojunction, indicating a much stronger interfacial electric field than that of the homojunction. (ii) Second, both SML and TMS have extrinsic contributions from interfacial disorder (including

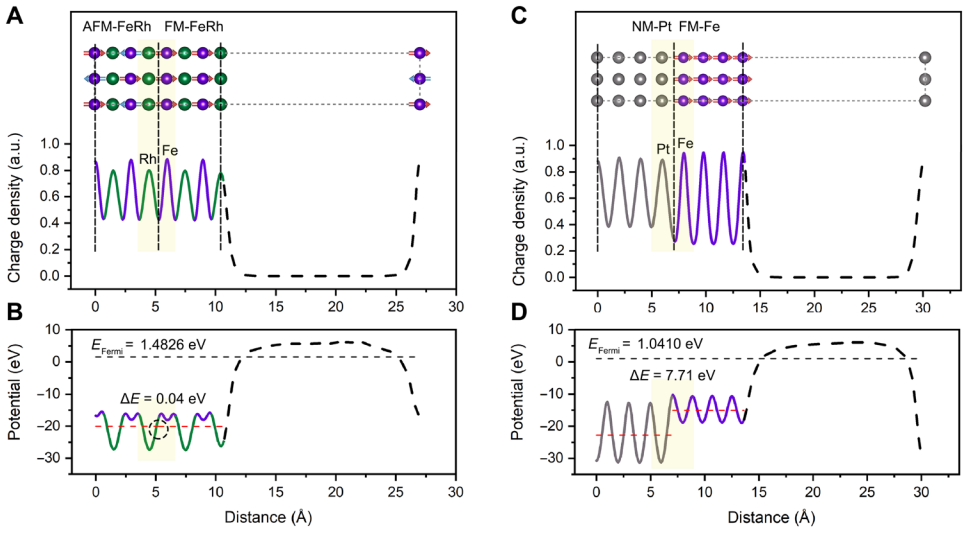

Fig. 5. First-principles calculations for spin homojunction and spin heterojunction. (**A**) Charge density and (**B**) planar potential for the FM-FeRh/AFM-FeRh homojunction. The interfacial potential difference is calculated to be 0.04 eV. (**C**) Charge density and (**D**) planar potential for the Pt/Fe heterojunction. The interfacial potential difference is calculated to be 7.71 eV.

defects, roughness, polycrystalline structure, etc.) (*17*, *21*). Compared with the common polycrystalline heterojunctions such as Fe/Pt, interfacial disorders in our single crystalline and epitaxial homojunction are negligible, which can also be verified by the HAADF-STEM image (Fig. 2F). Besides, SML originated from the bulk spin-orbit coupling (*57*) is little for our homojunction with conserved inversion symmetry and epitaxial interface. The conserved inversion symmetry and negligible interfacial spin-orbit coupling also exclude self-torques (*58*) from FM-FeRh in our FM-FeRh/AFM-FeRh homojunction. As a result, SML and TMS are negligible in our homojunction.

It should be noted that T can never reach 1, although the SML and TMS are ruled out for our homojunction. That is because the spin backflow should be taken into account in the definition of T (*25*) in bilayers, even in our ideal homojunction. By inserting a NiO layer to suppress the spin backflow by thermal magnon excitation, trilayer Pt/NiO/CoFeB junction realized $T = 1$ (*31*). Nevertheless, this design involves excitations of other spin carriers, indicating it is not a simple spin transmission process at the interface. The transparency of our spin homojunction has almost reached its physical limit based on the above two limits of $G_{eff}^{\uparrow\downarrow}$ (see a detailed explanation in Materials and Methods).

We report an FM-FeRh/AFM-FeRh spin homojunction for efficient spin-charge conversion, which has both practical and physical advances. On one hand, spin homojunction makes use of the analogous crystal structure and chemical environment, high single-crystallinity, and high flatness of FM-FeRh and AFM-FeRh, inherently reducing the interfacial spin-orbit coupling to eliminate SML and TMS at the interface. It leads to a crucially large T and ξ_{DL}^{j} of 0.75 and 0.34, demonstrating efficient spin-charge conversion in our spin homojunction, which gives fundamental enlightenment to energy-efficient spintronic devices. On the other hand, besides our FM-FeRh/AFM-FeRh spin homojunction, $CrBr_3$ and Mn_3GaN have the potential to construct FM-$CrBr_3$/AFM-$CrBr_3$ (*59*) and FM-Mn_3GaN/AFM-Mn_3GaN (*60*) spin homojunctions. These spin homojunctions provide simple and clean platforms to investigate spin-charge conversion phenomena (spin pumping, spin Hall effect, spin-orbit torques, spin Hall magnetoresistance, etc.) without the complicated influence of SML and TMS on interfacial spin transport.

MATERIALS AND METHODS

Sample preparations and measurement setups

The FM-FeRh/AFM-FeRh spin homojunction was grown on a single-crystal MgO(001) substrate by magnetron sputtering. The bottom 15-nm FM-FeRh and the upper 12-nm AFM-FeRh were deposited at 300°C at the Ar atmosphere of 0.4 and 0.7 Pa, respectively, followed by annealing at 750°C for 1 hour. All the samples were kept in a glove box with O_2 and H_2O < 0.01 parts per million to prevent degradation or oxidation. Four-terminal transport measurements were carried out in Physical Property Measurement System to collect ρ-T curves for characterizing the phase transition behavior of FeRh films. θ-2θ and φ-scan XRDs were carried out to obtain the crystal quality and grown modes of the homojunction. Atomic force microscopy was used to determine the roughness of FeRh films.

The cross-sectional HAADF-STEM and the EELS were carried out on an FEI Titan 80-300 electron microscopy equipped with a monochromator unit, a probe spherical aberration corrector, a postcolumn energy filter system (Gatan Tridiem 865 ER) and a Gatan 2k slow-scan charge-coupled device system, operating at 300 kV (*32*), combining an energy resolution of ~0.6 eV and a dispersion of 0.2 eV per channel with a spatial resolution of ~0.08 nm.

Spin homojunctions were patterned to 6 μm by 300 μm stripes using optimal lithography combined with Ar ion milling for spin pumping measurements. Then, Ti(10 nm)/Au(140 nm) ground-signal-ground CPW was thermally evaporated to conduct microwaves with ~50-ohm impedance match. Microwave of 19 dBm was introduced into the CPW from the microwave generator to excite FMR of the stripes. The actual microwave power on the stripe was measured to be 7.5 dBm by a thermal-equivalent method (fig. S4). The voltage across the stripe was captured via a nanovoltmeter when sweeping the magnetic field, which is composed of the ISHE signal

from spin pumping and the AMR rectification signal. These stripes were located in the gap between the ground line and the signal line, leading to a $\boldsymbol{h}_{oop}$ excitation configuration for feasible distinguishment between the ISHE signal and the AMR signal via angle-dependent measurements (*39*).

COMSOL simulations

The microwave magnetic field intensity distribution in CPW was simulated with a radio frequency module (electromagnetic waves and frequency domain) in COMSOL Multiphysics. Propagation region was bound by scattering boundary conditions. To simplify the model, Ti layer was ignored, and Au layer was approximated by transition boundary conditions with a thickness of 140 nm. We used lumped exports, the known impedance of 50 ohms, and microwave power of 7.5 dBm to excite the CPW. Because of the relatively small thickness of Au, the meshing was chosen finer around the stripe. Then, magnetic field intensity distribution around the CPW could be obtained (fig. S4). The micromagnetic magnetic field $\mu_0 h^0$ around the stripe was calculated to be 0.052 mT.

Density functional theory calculations

All the first-principles calculations were performed in Vienna ab initio simulation package, with the Perdew-Burke-Ernzerhof functional. The calculations were based on a cutoff energy of 500 eV. The γ-centered *k*-point mesh of 24 × 24 × 1 was used in the calculations of both FeRh homojunction and Pt/Fe heterostructure. A vacuum layer larger than 15 Å was adopted in all calculations of thin films, which is large enough for the structures.

Principles of the spin pumping measurements and determination of ξ^j_{DL}

The spin pumping process in FM-FeRh/AFM-FeRh involves the FMR of FM-FeRh, pumping spin current into the adjacent AFM-FeRh, which is then converted to charge current by ISHE. The Landau-Lifshitz-Gilbert (LLG) equation is modified by the spin pumping process as (*61*)

$$\frac{d\boldsymbol{m}}{dt} = -\gamma(\boldsymbol{m}\times\boldsymbol{h}_{eff}) + \alpha_{Gil}\left(\boldsymbol{m}\times\frac{d\boldsymbol{m}}{dt}\right) + \frac{\gamma}{VM_s}\boldsymbol{I}_s \quad (9)$$

where $\boldsymbol{m}$ is the magnetic moment and $\boldsymbol{h}_{eff}$ is the localized effective magnetic field on $\boldsymbol{m}$. γ is the gyromagnetic ratio, α_{Gil} is the intrinsic Gilbert damping, and M_s and V are the saturation magnetization and the volume of FM-FeRh. $\boldsymbol{I}_s$ is the total spin current, which reads $\boldsymbol{I}_s = \boldsymbol{I}_s^{pump} - \boldsymbol{I}_s^{back}$, considering the spin backflow $\boldsymbol{I}_s^{back}$. By substituting α_{Gil} by the effective damping constant of the FM-FeRh/AFM-FeRh homojunction $\alpha_{FM/AFM}$, the last term in Eq. 9 can be combined with the second term, which results in the same form as the original LLG equation (*61*)

$$\frac{d\boldsymbol{M}}{dt} = -\gamma\boldsymbol{M}\times\mu_0\boldsymbol{H}_{eff} + \frac{\alpha_{FM/AFM}}{|\boldsymbol{M}|}\boldsymbol{M}\times\frac{d\boldsymbol{M}}{dt} \quad (10)$$

where $\boldsymbol{M}$ is the magnetization vector and $d\boldsymbol{M}/dt$ is its time derivative. $\boldsymbol{H}_{eff}$ is the effective magnetic field and μ_0 is the vacuum permeability. We define two Cartesian coordinate systems as shown in fig. S12. x', y', and z' axes are based on the direction of magnetization x', while x, y, and z axes are related to the direction of microwave current x. The microwave current $\boldsymbol{j}_x(t)$ is along the stripe, generating inductive current $\boldsymbol{j}_{FM}(t)$ and $\boldsymbol{j}_{AFM}(t)$ in FM-FeRh and AFM-FeRh in the same direction, respectively. φ_M/φ_H denotes the angle between the magnetization/magnetic field and x axis. Two main excitations are involved, the OOP microwave magnetic field $\boldsymbol{h}_{OOP}$ from CPW and the IP Oersted field $\boldsymbol{h}_{IP}$ due to $\boldsymbol{j}_{AFM}(t)$. In the coordinate of (x', y', z'), $\boldsymbol{M}= (M_x, m_y e^{i\omega t}, m_z e^{i\omega t})$, $\boldsymbol{h}_{OOP} = e^{i\omega t}(0, 0, h^0)$, $\boldsymbol{h}_{IP} = e^{i\omega t}(h_{Oe}\sin\varphi_M, h_{Oe}\cos\varphi_M, 0)$, where ω is the angle frequency of microwave with $\omega = 2\pi f$. Considering the external constant magnetic field H and the perpendicular anisotropic effective field, the total effective field $\boldsymbol{H}_{eff} = (H^x_{eff}, H^y_{eff}, H^z_{eff})$ is (*62*)

$$H^x_{eff} = H\cos(\varphi_M - \varphi_H) + h_{Oe}\sin\varphi_M e^{i\omega t} \quad (11)$$

$$H^y_{eff} = h_{Oe}\cos\varphi_M e^{i\omega t} \quad (12)$$

$$H^z_{eff} = -M_{eff}\frac{m_z e^{i\omega t}}{M_x} + h^0 e^{iwt} \quad (13)$$

Solving Eqs. 10 to 13, one can obtain the resonance condition, namely, the Kittel formulation $f = \frac{\gamma}{2\pi}\sqrt{H_R(H_R + M_{eff})}$, where f and H_R are the frequency of microwave and corresponding resonance field. Note that the IP anisotropy is negligible in our FM-FeRh layer compared with M_{eff} and H_R at a relative high microwave frequency of 17 GHz (fig. S6), and thus is left out for simplicity. In this case, $\varphi_M \approx \varphi_H$. Assuming $\alpha_{FM/AFM} << 1$, $M_x \approx M_s$, we relate $\boldsymbol{M}$ with $\boldsymbol{h}_{OOP}$ and $\boldsymbol{h}_{IP}$ by the dynamical magnetic complex susceptibility χ (*35*)

$$\begin{pmatrix} m_y \\ m_z \end{pmatrix} = \begin{pmatrix} \chi^{IP} & -i\chi_a^{OOP} \\ i\chi_a^{IP} & \chi^{OOP} \end{pmatrix}\begin{pmatrix} h_{Oe}\cos\varphi_M e^{i\Phi_1} \\ h^0 e^{i\Phi_2} \end{pmatrix} \quad (14)$$

Here, $\chi^{OOP}(\chi_a^{OOP})$ is the complex diagonal (off-diagonal) dynamics magnetic susceptibility due to h^0. $\chi^{IP}(\chi_a^{IP})$ is the complex diagonal (off-diagonal) dynamics magnetic susceptibility due to h_{Oe}. Φ_1 (Φ_2) represents the phase difference between magnetization dynamics and h_{Oe} (h^0). Eq. 14 results in

$$Re(m_y) = Re(\chi^{IP})h_{Oe}\cos\varphi_M\cos\Phi_1 - Im(\chi^{IP})h_{Oe}\cos\varphi_M\sin\Phi_1 + Re(\chi_a^{OOP})h^0\sin\Phi_2 + Im(\chi_a^{OOP})h^0\cos\Phi_2$$

$$Im(m_y) = Im(\chi^{IP})h_{Oe}\cos\varphi_M\cos\Phi_1 + Re(\chi^{IP})h_{Oe}\cos\varphi_M\sin\Phi_1 + Im(\chi_a^{OOP})h^0\sin\Phi_2 - Re(\chi_a^{OOP})h^0\cos\Phi_2$$

$$Re(m_z) = -Im(\chi_a^{IP})h_{Oe}\cos\varphi_M\cos\Phi_1 - Re(\chi_a^{IP})h_{Oe}\cos\varphi_M\sin\Phi_1 - Im(\chi^{OOP})h^0\sin\Phi_2 + Re(\chi^{OOP})h^0\cos\Phi_2$$

$$Im(m_z) = Re(\chi_a^{IP})h_{Oe}\cos\varphi_M\cos\Phi_1 - Im(\chi_a^{IP})h_{Oe}\cos\varphi_M\sin\Phi_1 + Re(\chi^{OOP})h^0\sin\Phi_2 + Im(\chi^{OOP})h^0\cos\Phi_2 \quad (15)$$

where χ can be decomposed into real parts and imaginary parts and reads (*62*)

$$Re(\chi^{IP}) = -\frac{H_1(H_1^R H_2^R - H_1 H_2)M_s}{(H_1^R H_2^R - H_1 H_2)^2 + \alpha_{FM/AFM}^2 H_1^R H_2^R (H_1 + H_2)^2}$$

$$Im(\chi^{IP}) = \frac{\alpha_{FM/AFM}\sqrt{H_1^R H_2^R}(H_1^R H_2^R + H_1 H_2)M_s}{(H_1^R H_2^R - H_1 H_2)^2 + \alpha_{FM/AFM}^2 H_1^R H_2^R (H_1 + H_2)^2}$$

$$Re(\chi_a^{IP}) = \frac{\sqrt{H_1^R H_2^R}(H_1^R H_2^R - H_1 H_2) M_s}{(H_1^R H_2^R - H_1 H_2)^2 + \alpha_{FM/AFM}^2 H_1^R H_2^R (H_1 + H_2)^2}$$

$$Im(\chi_a^{IP}) = -\frac{\alpha_{FM/AFM} H_1^R H_2^R (H_1 + H_2) M_s}{(H_1^R H_2^R - H_1 H_2)^2 + \alpha_{FM/AFM}^2 H_1^R H_2^R (H_1 + H_2)^2}$$

$$Re(\chi^{OOP}) = -\frac{H_2 (H_1^R H_2^R - H_1 H_2) M_s}{(H_1^R H_2^R - H_1 H_2)^2 + \alpha_{FM/AFM}^2 H_1^R H_2^R (H_1 + H_2)^2}$$

$$Im(\chi^{OOP}) = \frac{\alpha_{FM/AFM} \sqrt{H_1^R H_2^R}(H_1^R H_2^R + H_1 H_2) M_s}{(H_1^R H_2^R - H_1 H_2)^2 + \alpha_{FM/AFM}^2 H_1^R H_2^R (H_1 + H_2)^2}$$

$$Re(\chi_a^{OOP}) = \frac{\sqrt{H_1^R H_2^R}(H_1^R H_2^R - H_1 H_2) M_s}{(H_1^R H_2^R - H_1 H_2)^2 + \alpha_{FM/AFM}^2 H_1^R H_2^R (H_1 + H_2)^2}$$

$$Im(\chi_a^{OOP}) = -\frac{\alpha_{FM/AFM} H_2^R (H_1 + H_2) M_s}{(H_1^R H_2^R - H_1 H_2)^2 + \alpha_{FM/AFM}^2 H_1^R H_2^R (H_1 + H_2)^2} \quad (16)$$

$$H_1 = H + M_{eff}, H_2 = H, H_1^R = H_R + M_{eff}, H_2^R = H_R$$

The ISHE voltage V_{ISHE} can be expressed as the following with negligible SML (*35*)

$$V_{ISHE} = R I_c = R \frac{2e}{\hbar} \theta_{SH} J_s w \lambda_s \tanh \frac{d_{AFM}}{2\lambda_s} \sin\varphi_M \quad (17)$$

For systems with substantial SML, please refer to the work by Krishnia *et al.* with T and SML included (*63*), R is the resistance of the FM-FeRh/AFM-FeRh homojunction, I_c is the ISHE-induced charge current, and J_s is the magnitude of the spin current at the interface. e and $\hbar$ are the electron charge and the reduced Planck constant. w is the width of the stripe. d_{AFM}, θ_{SH}, and λ_s are the thickness, the spin Hall angle, and the spin diffusion length of the AFM-FeRh layer, respectively. ρ_{AFM} is the resistivity of the AFM-FeRh. Considering $d_{AFM} >> \lambda_s$, $\tanh \frac{d_{AFM}}{2\lambda_s} \approx 1$. J_s is determined by (*35*)

$$J_s = \frac{\hbar^2 \omega}{2e^2} G_{eff}^{\uparrow\downarrow} \frac{1}{M_s^2} [Im(m_y) Re(m_z) - Im(m_z) Re(m_y)] \quad (18)$$

As a result, for φ_M-dependent spin pumping measurements

$$V_{ISHE} \sim [Im(m_y) Re(m_z) - Im(m_z) Re(m_y)] \sin\varphi_M \quad (19)$$

Merging similar items containing h_{Oe} as V_{ISHE}^{IP} and h^0 as V_{ISHE}^{OOP}, we have $V_{ISHE} = V_{ISHE}^{IP} + V_{ISHE}^{OOP}$, and the angle dependence of V_{ISHE}^{IP} and V_{ISHE}^{OOP} can be expressed as

$$V_{ISHE}^{IP} = -T\theta_{SH} \frac{Rwhf}{2\rho_{AFM} e M_s^2} \left[Im(\chi^{IP}) Im(\chi_a^{IP}) + Re(\chi^{IP}) Re(\chi_a^{IP}) \right] [h_{Oe}]^2 \cos^2\varphi_M \sin\varphi_M \quad (20)$$

$$V_{ISHE}^{OOP} = -T\theta_{SH} \frac{Rwhf}{2\rho_{AFM} e M_s^2} \left[Im(\chi^{OOP}) Im(\chi_a^{OOP}) + Re(\chi^{OOP}) Re(\chi_a^{OOP}) \right] [h^0]^2 \sin\varphi_M \quad (21)$$

Considering that $Re(\chi)$ and $Im(\chi)$ have antisymmetric and symmetric line shapes, respectively, we conclude that ISHE only contributes to the symmetric line shape.

For AMR rectification volage, it can be expressed as (*62*)

$$V_{AMR} = -\frac{\Delta\rho j_{FM} L}{2 M_s} Re(m_y) \sin 2\varphi_M \quad (22)$$

Here, $\Delta\rho$ is the resistivity difference between the magnetization parrel to the current and the magnetization perpendicular to the current. L is the length of the stripe, equaling 300 μm. Similarly, we have $V_{AMR} = V_{AMR}^{IP} + V_{AMR}^{OOP}$, and

$$V_{AMR}^{IP} = -\frac{\Delta\rho L}{2 M_s} \left[Re(\chi^{IP}) \cos\Phi_1 - Im(\chi^{IP}) \sin\Phi_1 \right] j_{FM} h_{Oe} \cos^2\varphi_M \sin\varphi_M \quad (23)$$

$$V_{AMR}^{OOP} = -\frac{\Delta\rho L}{2 M_s} [Re(\chi_a^{OOP}) \sin\Phi_2 + Im(\chi_a^{OOP}) \cos\Phi_2] j_{FM} h^0 \sin 2\varphi_M \quad (24)$$

It is clear that AMR rectification contributes to both the symmetric and the antisymmetric line shapes. Consequently, we can separate AMR and ISHE signals from angle-dependent spin pumping measurements by $V = V_{asym} L_{asym} + V_{sym} L_{sym}$, where $L_{sym} = -4\Delta H(H - H_R)/[4(H - H_R)^2 + \Delta H^2]$ and $L_{asym} = \Delta H^2/[4(H - H_R)^2 + \Delta H^2]$ are the symmetric and the antisymmetric Lorentz line shapes

$$V_{asym} = U_{AMR}^{IP,asym} + U_{AMR}^{OOP,asym} = A\cos^2\varphi_M \sin\varphi_M + B\sin 2\varphi_M$$

$$V_{sym} = U_{ISHE}^{OOP,sym} + \left(U_{AMR}^{IP,sym} + U_{ISHE}^{IP,sym} \right) + U_{AMR}^{OOP,sym} = C\sin\varphi_M + D\cos^2\varphi_M \sin\varphi_M + E\sin 2\varphi_M \quad (25)$$

For $\varphi_M = 90°$, only V_{ISHE}^{OOP} contributes to the voltage V. On the basis of Eq. 21, we substitute the V_{ISHE}^{OOP} by data shown in Fig. 3C. $R = 1989$ ohms, $w = 6$ μm, $h = 6.626 \times 10^{-34}$ J·s, $f = 17$ GHz, $\rho_{AFM} = 144$ microhm·cm, $e = 1.6 \times 10^{19}$ C, $\mu_0 M_s = 926.29$ mT, and $\mu_0 h^0 = 0.052$ mT. Last, θ_{SH} turns out to be 0.46. After that, we determine ξ_{DL}^j as

$$\xi_{DL}^j = T\theta_{SH} = 0.34 \quad (26)$$

Estimation on the upper limitation of the interfacial transparency based on the Sharvin conductance

Sharvin conductance means the contact conductance dominated by the Sharvin mechanism, when the size of microcontacts is less than the mean free path λ of electron (*64*). For a microcontact of area a_i, local Sharvin conductance $G_i = a_i/\lambda\bar{\rho}$, where $\bar{\rho} = (\rho_1 + \rho_2)/2$ (*64*). ρ_1 and ρ_2 are the specific resistivities of contacting surfaces. The resistivity of our FM-FeRh and AFM-FeRh are 66 and 144 microhm·cm, respectively; hence, $\bar{\rho} \sim 0.75\ \rho_{AFM}$. For an interface of area A, the Sharvin conductance reads

$$G_{sh} = \frac{\sum G_i}{A} = \frac{\sum a_i}{A} \frac{1}{\lambda\bar{\rho}} \quad (27)$$

Here, $\sum a_i/A$ is influenced by the roughness of the interface. We estimate $\sum a_i/A$ to be close to 1, considering that the roughness of

our FM-FeRh/AFM-FeRh homojunction is negligibly small, verified by both the HAADF-STEM image and atomic force microscope measurements. Note that the spin diffusion length λ_s is always larger than the mean free path λ of the electron (*18*). By simply considering $\lambda_s = (1 - 1.5)\lambda$, we can roughly estimate that $G_{sh} \sim (1.3 \text{ to } 1.8)\, G_{AFM}$. On the basis of $G_{eff}^{\uparrow\downarrow} < (G_{sh} G_{AFM}) / (2G_{sh} + G_{AFM})$, we have the upper limit of $G_{eff}^{\uparrow\downarrow} < (0.25 \text{ to } 0.27) \times 10^{15}$, which is close to our $G_{eff}^{\uparrow\downarrow} = 0.259 \times 10^{15}$. As a result, the $G_{eff}^{\uparrow\downarrow}$ of our spin homojunction and concomitant with the interfacial transparency $T \propto G_{eff}^{\uparrow\downarrow}$ has almost reached its physical limit.

SUPPLEMENTARY MATERIALS

Supplementary material for this article is available at https://science.org/doi/10.1126/sciadv.abq2742

REFERENCES AND NOTES

1. J. Wunderlich, B. G. Park, A. C. Irvine, L. P. Zârbo, E. Rozkotová, P. Nemec, V. Novák, J. Sinova, T. Jungwirth, Spin Hall effect transistor. *Science* **330**, 1801–1804 (2010).
2. L. Zhu, L. Zhu, M. Sui, D. C. Ralph, R. A. Buhrman, Variation of the giant intrinsic spin Hall conductivity of Pt with carrier lifetime. *Sci. Adv.* **5**, eaav8025 (2019).
3. L. Liu, C. F. Pai, Y. Li, H. W. Tseng, D. C. Ralph, R. A. Buhrman, Spin-torque switching with the giant spin Hall effect of tantalum. *Science* **336**, 555–558 (2012).
4. M. Obstbaum, M. Decker, A. K. Greitner, M. Haertinger, T. N. G. Meier, M. Kronseder, K. Chadova, S. Wimmer, D. Ködderitzsch, H. Ebert, C. H. Back, Tuning spin Hall angles by alloying. *Phys. Rev. Lett.* **117**, 167204 (2016).
5. L. Zhu, D. C. Ralph, R. A. Buhrman, Highly efficient spin-current generation by the spin Hall effect in $Au_{1-x}Pt_x$. *Phys. Rev. Appl.* **10**, 031001 (2018).
6. Y. Ou, D. C. Ralph, R. A. Buhrman, Strong enhancement of the spin Hall effect by spin fluctuations near the curie point of Fe_xPt_{1-x} Alloys. *Phys. Rev. Lett.* **120**, 097203 (2018).
7. D. MacNeill, G. M. Stiehl, M. H. D. Guimaraes, R. A. Buhrman, J. Park, D. C. Ralph, Control of spin-orbit torques through crystal symmetry in WTe_2/ferromagnet bilayers. *Nat. Phys.* **13**, 300–305 (2017).
8. Q. Shao, G. Yu, Y. W. Lan, Y. Shi, M. Y. Li, C. Zheng, X. Zhu, L. J. Li, P. K. Amiri, K. L. Wang, Strong rashba-edelstein effect-induced spin-orbit torques in monolayer transition metal dichalcogenide/ferromagnet bilayers. *Nano Lett.* **16**, 7514–7520 (2016).
9. X. Huang, S. Sayed, J. Mittelstaedt, S. Susarla, S. Karimeddiny, L. Caretta, H. Zhang, V. A. Stoica, T. Gosavi, F. Mahfouzi, Q. Sun, P. Ercius, N. Kioussis, S. Salahuddin, D. C. Ralph, R. Ramesh, Novel spin–orbit torque generation at room temperature in an all-oxide epitaxial $La_{0.7}Sr_{0.3}MnO_3/SrIrO_3$ system. *Adv. Mater.* **33**, 2008269 (2021).
10. W. Zhang, W. Han, S. H. Yang, Y. Sun, Y. Zhang, B. Yan, S. S. P. Parkin, Giant facet-dependent spin-orbit torque and spin Hall conductivity in the triangular antiferromagnet IrMn3. *Sci. Adv.* **2**, e1600759 (2016).
11. C. Song, R. Zhang, L. Liao, Y. Zhou, X. Zhou, R. Chen, Y. You, X. Chen, F. Pan, Spin-orbit torques: Materials, mechanisms, performances, and potential applications. *Prog. Mater. Sci.* **118**, 100761 (2021).
12. S. O. Valenzuela, M. Tinkham, Direct electronic measurement of the spin Hall effect. *Nature* **442**, 176–179 (2006).
13. L. Liu, O. J. Lee, T. J. Gudmundsen, D. C. Ralph, R. A. Buhrman, Current-induced switching of perpendicularly magnetized magnetic layers using spin torque from the spin Hall effect. *Phys. Rev. Lett.* **109**, 096602 (2012).
14. H. Nakayama, M. Althammer, Y. T. Chen, K. Uchida, Y. Kajiwara, D. Kikuchi, T. Ohtani, S. Geprägs, M. Opel, S. Takahashi, R. Gross, G. E. W. Bauer, S. T. B. Goennenwein, E. Saitoh, Spin Hall magnetoresistance induced by a nonequilibrium proximity effect. *Phys. Rev. Lett.* **110**, 206601 (2013).
15. K. Chen, S. Zhang, Spin pumping in the presence of spin-orbit coupling. *Phys. Rev. Lett.* **114**, 126602 (2015).
16. L. Zhu, D. C. Ralph, R. A. Buhrman, Spin-orbit torques in heavy-metal-ferromagnet bilayers with varying strengths of interfacial spin-orbit coupling. *Phys. Rev. Lett.* **122**, 077201 (2019).
17. K. Gupta, R. J. H. Wesselink, R. Liu, Z. Yuan, P. J. Kelly, Disorder dependence of interface spin memory loss. *Phys. Rev. Lett.* **124**, 087702 (2020).
18. X. Tao, Q. Liu, B. Miao, R. Yu, Z. Feng, L. Sun, B. You, J. Du, K. Chen, S. Zhang, L. Zhang, Z. Yuan, D. Wu, H. Ding, Self-consistent determination of spin Hall angle and spin diffusion length in Pt and Pd: The role of the interface spin loss. *Sci. Adv.* **4**, eaat1670 (2018).
19. J. C. Rojas-Sánchez, N. Reyren, P. Laczkowski, W. Savero, J. P. Attané, C. Deranlot, M. Jamet, J. M. George, L. Vila, H. Jaffrès, Spin pumping and inverse spin Hall effect in platinum: The essential role of spin-memory loss at metallic interfaces. *Phys. Rev. Lett.* **112**, 106602 (2014).
20. K. D. Belashchenko, A. A. Kovalev, M. Van Schilfgaarde, Theory of spin loss at metallic interfaces. *Phys. Rev. Lett.* **117**, 207204 (2016).
21. L. Zhu, L. Zhu, D. C. Ralph, R. A. Buhrman, Origin of strong two-magnon scattering in heavy-metal/ferromagnet/oxide heterostructures. *Phys. Rev. Appl.* **13**, 034038 (2020).
22. L. Zhu, D. C. Ralph, R. A. Buhrman, Effective spin-mixing conductance of heavy-metal-ferromagnet interfaces. *Phys. Rev. Lett.* **123**, 057203 (2019).
23. S. N. Panda, S. Mondal, J. Sinha, S. Choudhury, A. Barman, All-optical detection of interfacial spin transparency from spin pumping in β-Ta/CoFeB thin films. *Sci. Adv.* **5**, eaav7200 (2019).
24. W. Zhang, W. Han, X. Jiang, S. H. Yang, S. S. P. Parkin, Role of transparency of platinum-ferromagnet interfaces in determining the intrinsic magnitude of the spin Hall effect. *Nat. Phys.* **11**, 496–502 (2015).
25. C. F. Pai, Y. Ou, L. H. Vilela-Leão, D. C. Ralph, R. A. Buhrman, Dependence of the efficiency of spin Hall torque on the transparency of Pt/ferromagnetic layer interfaces. *Phys. Rev. B* **92**, 064426 (2015).
26. M. Weiler, M. Althammer, M. Schreier, J. Lotze, M. Pernpeintner, S. Meyer, H. Huebl, R. Gross, A. Kamra, J. Xiao, Y. T. Chen, H. Jiao, G. E. W. Bauer, S. T. B. Goennenwein, Experimental test of the spin mixing interface conductivity concept. *Phys. Rev. Lett.* **111**, 176601 (2013).
27. L. Zhu, D. C. Ralph, R. A. Buhrman, Enhancement of spin transparency by interfacial alloying. *Phys. Rev. B.* **99**, 180404 (2019).
28. Y. Ou, S. Shi, D. C. Ralph, R. A. Buhrman, Strong spin Hall effect in the antiferromagnet PtMn. *Phys. Rev. B.* **93**, 220405 (2016).
29. C. Du, H. Wang, F. Yang, P. C. Hammel, Enhancement of pure spin currents in spin pumping $Y_3Fe_5O_{12}$/Cu/ metal trilayers through spin conductance matching. *Phys. Rev. Appl.* **1**, 044004 (2014).
30. A. Anadón, R. Guerrero, J. A. Jover-Galtier, A. Gudín, J. M. Díez Toledano, P. Olleros-Rodríguez, R. Miranda, J. Camarero, P. Perna, Spin-orbit torque from the introduction of Cu interlayers in Pt/Cu/Co/Pt nanolayered structures for spintronic devices. *ACS Appl. Nano Mater.* **4**, 487–492 (2021).
31. L. Zhu, L. Zhu, R. A. Buhrman, Fully spin-transparent magnetic interfaces enabled by the insertion of a thin paramagnetic NiO layer. *Phys. Rev. Lett.* **126**, 107204 (2021).
32. X. Z. Chen, J. F. Feng, Z. C. Wang, J. Zhang, X. Y. Zhong, C. Song, L. Jin, B. Zhang, F. Li, M. Jiang, Y. Z. Tan, X. J. Zhou, G. Y. Shi, X. F. Zhou, X. D. Han, S. C. Mao, Y. H. Chen, X. F. Han, F. Pan, Tunneling anisotropic magnetoresistance driven by magnetic phase transition. *Nat. Commun.* **8**, 449 (2017).
33. T. Nan, Y. Lee, S. Zhuang, Z. Hu, J. D. Clarkson, X. Wang, C. Ko, H. Choe, Z. Chen, D. Budil, J. Wu, S. Salahuddin, J. Hu, R. Ramesh, N. Sun, Electric-field control of spin dynamics during magnetic phase transitions. *Sci. Adv.* **6**, eabd2613 (2020).
34. X. Marti, I. Fina, C. Frontera, J. Liu, P. Wadley, Q. He, R. J. Paull, J. D. Clarkson, J. Kudrnovský, I. Turek, J. Kuneš, D. Yi, J. Chu, C. T. Nelson, L. You, E. Arenholz, S. Salahuddin, J. Fontcuberta, T. Jungwirth, R. Ramesh, Room-temperature antiferromagnetic memory resistor. *Nat. Mater.* **13**, 367–374 (2014).
35. Y. Wang, M. M. Decker, T. N. G. Meier, X. Chen, C. Song, T. Grünbaum, W. Zhao, J. Zhang, L. Chen, C. H. Back, Spin pumping during the antiferromagnetic–ferromagnetic phase transition of iron–rhodium. *Nat. Commun.* **11**, 275 (2020).
36. J. C. Rojas-Sánchez, A. Fert, Compared efficiencies of conversions between charge and spin current by spin-orbit interactions in two- and three-dimensional systems. *Phys. Rev. Appl.* **11**, 054049 (2019).
37. M. Jiang, X. Z. Chen, X. J. Zhou, Y. Y. Wang, F. Pan, C. Song, Influence of film composition on the transition temperature of FeRh films. *J. Cryst. Growth* **438**, 19–24 (2016).
38. Y. Tserkovnyak, A. Brataas, G. E. W. Bauer, Enhanced Gilbert damping in thin ferromagnetic films. *Phys. Rev. Lett.* **88**, 117601 (2002).
39. M. Obstbaum, M. Härtinger, H. G. Bauer, T. Meier, F. Swientek, C. H. Back, G. Woltersdorf, Inverse spin Hall effect in$Ni_{81}Fe_{19}$/normal-metal bilayers. *Phys. Rev. B.* **89**, 060407 (2014).
40. J. Cheng, K. He, M. Yang, Q. Liu, R. Yu, L. Sun, J. Ding, B. Miao, M. Wu, H. F. Ding, Quantitative estimation of thermoelectric contributions in spin pumping signals through microwave photoresistance measurements. *Phys. Rev. B* **103**, 014415 (2021).
41. P. Noël, M. Cosset-Cheneau, V. Haspot, V. Maurel, C. Lombard, M. Bibes, A. Barthelemy, L. Vila, J. P. Attané, Negligible thermal contributions to the spin pumping signal in ferromagnetic metal-platinum bilayers. *J. Appl. Phys.* **127**, 163907 (2020).
42. R. Modak, M. Murata, D. Hou, A. Miura, R. Iguchi, B. Xu, R. Guo, J. Shiomi, Y. Sakuraba, K. I. Uchida, Phase-transition-induced giant Thomson effect for thermoelectric cooling. *Appl. Phys. Rev.* **9**, 011414 (2022).
43. H. Saglam, J. C. Rojas-Sanchez, S. Petit, M. Hehn, W. Zhang, J. E. Pearson, S. Mangin, A. Hoffmann, Independence of spin-orbit torques from the exchange bias direction in$Ni_{81}Fe_{19}$/IrMn bilayers. *Phys. Rev. B.* **98**, 094407 (2018).
44. L. Liu, T. Moriyama, D. C. Ralph, R. A. Buhrman, Spin-torque ferromagnetic resonance induced by the spin Hall effect. *Phys. Rev. Lett.* **106**, 036601 (2011).
45. Z. Qiu, K. Ando, K. Uchida, Y. Kajiwara, R. Takahashi, H. Nakayama, T. An, Y. Fujikawa, E. Saitoh, Spin mixing conductance at a well-controlled platinum/yttrium iron garnet interface. *Appl. Phys. Lett.* **103**, 092404 (2013).

46. A. Kumar, S. Akansel, H. Stopfel, M. Fazlali, J. Åkerman, R. Brucas, P. Svedlindh, Spin transfer torque ferromagnetic resonance induced spin pumping in the Fe/Pd bilayer system. *Phys. Rev. B.* **95**, 064406 (2017).
47. A. J. Berger, E. R. J. Edwards, H. T. Nembach, O. Karis, M. Weiler, T. J. Silva, Determination of the spin Hall effect and the spin diffusion length of Pt from self-consistent fitting of damping enhancement and inverse spin-orbit torque measurements. *Phys. Rev. B* **98**, 024402 (2018).
48. B. Sahoo, K. Roy, P. Gupta, A. Mishra, B. Satpati, B. B. Singh, S. Bedanta, Spin pumping and inverse spin Hall effect in iridium oxide. *Adv. Quantum Technol.* **4**, 2000146 (2021).
49. L. Huang, S. He, Q. J. Yap, S. Ter Lim, Engineering magnetic heterostructures to obtain large spin Hall efficiency for spin-orbit torque devices. *Appl. Phys. Lett.* **113**, 022402 (2018).
50. W. Zhang, M. B. Jungfleisch, F. Freimuth, W. Jiang, J. Sklenar, J. E. Pearson, J. B. Ketterson, Y. Mokrousov, A. Hoffmann, All-electrical manipulation of magnetization dynamics in a ferromagnet by antiferromagnets with anisotropic spin Hall effects. *Phys. Rev. B* **92**, 144405 (2015).
51. L. Zhu, K. Sobotkiewich, X. Ma, X. Li, D. C. Ralph, R. A. Buhrman, Strong damping-like spin-orbit torque and tunable dzyaloshinskii–Moriya interaction generated by low-resistivity $Pd_{1-x}Pt_x$ alloys. *Adv. Funct. Mater.* **29**, 1805822 (2019).
52. B. B. Singh, S. Bedanta, Large spin Hall angle and spin-mixing conductance in the highly resistive antiferromagnet Mn_2Au. *Phys. Rev. Appl.* **13**, 044020 (2020).
53. H. Hayashi, A. Musha, H. Sakimura, K. Ando, Spin-orbit torques originating from the bulk and interface in Pt-based structures. *Phys. Rev. Res.* **3**, 013042 (2021).
54. K. Rogdakis, A. Sud, M. Amado, C. M. Lee, L. McKenzie-Sell, K. R. Jeon, M. Cubukcu, M. G. Blamire, J. W. A. Robinson, L. F. Cohen, H. Kurebayashi, Spin transport parameters of NbN thin films characterized by spin pumping experiments. *Phys. Rev. Mater.* **3**, 014406 (2019).
55. H. Wang, C. Du, P. C. Hammel, F. Yang, Comparative determination of $Y_3Fe_5O_{12}$/Pt interfacial spin mixing conductance by spin-Hall magnetoresistance and spin pumping. *Appl. Phys. Lett.* **110**, 062402 (2017).
56. Y. A. Bychkov, E. I. Rashba, Oscillatory effects and the magnetic susceptibility of carriers in inversion layers. *J. Phys. C Solid State Phys.* **17**, 6039–6045 (1984).
57. M. Lim, H. W. Lee, Spin-memory loss induced by bulk spin-orbit coupling at ferromagnet/heavy-metal interfaces. *Appl. Phys. Lett.* **118**, 042408 (2021).
58. D. Céspedes-Berrocal, H. Damas, S. Petit-Watelot, D. Maccariello, P. Tang, A. Arriola-Córdova, P. Vallobra, Y. Xu, J. L. Bello, E. Martin, S. Migot, J. Ghanbaja, S. Zhang, M. Hehn, S. Mangin, C. Panagopoulos, V. Cros, A. Fert, J. C. Rojas-Sánchez, Current-induced spin torques on single GdFeCo magnetic layers. *Adv. Mater.* **33**, e2007047 (2021).
59. W. Chen, Z. Sun, Z. Wang, L. Gu, X. Xu, S. Wu, C. Gao, Direct observation of van der Waals stacking–dependent interlayer magnetism. *Science* **366**, 983–987 (2019).
60. T. Hajiri, S. Ishino, K. Matsuura, H. Asano, Electrical current switching of the noncollinear antiferromagnet Mn_3GaN. *Appl. Phys. Lett.* **115**, 052403 (2019).
61. Y. Tserkovnyak, A. Brataas, G. E. W. Bauer, Spin pumping and magnetization dynamics in metallic multilayers. *Phys. Rev. B.* **66**, 224403 (2002).
62. L. Chen, M. Decker, M. Kronseder, R. Islinger, M. Gmitra, D. Schuh, D. Bougeard, J. Fabian, D. Weiss, C. H. Back, Robust spin-orbit torque and spin-galvanic effect at the Fe/GaAs (001) interface at room temperature. *Nat. Commun.* **7**, 13802 (2016).
63. S. Krishnia, Y. Sassi, F. Ajejas, N. Reyren, S. Collin, A. Fert, J.-M. George, V. Cros, H. Jaffres, Large interfacial Rashba interaction and giant spin-orbit torques in atomically thin metallic heterostructures. arXiv:2205.08486 (2022).
64. C. Zhai, D. Hanaor, G. Proust, L. Brassart, Y. Gan, Interfacial electro-mechanical behaviour at rough surfaces. *Extrem. Mech. Lett.* **9**, 422–429 (2016).

Acknowledgments

Funding: This work is supported by the National Key Research and Development Program of China (MOST) (grant no. 2021YFB3601301), the National Natural Science Foundation of China (grant nos. 52225106, 62174095, and 51871130), and the Natural Science Foundation of Beijing, China (grant no. JQ20010). C.S. acknowledges the support of Beijing Innovation Center for Future Chip (ICFC), Tsinghua University. **Author contributions:** L.H., Y. Wang, C.S., and F.P. initiated the research and designed the experiments. L.H. grew films and prepared samples, and L.H. and Y. Wang carried out measurements. W.Z performed DFT calculations. R.Z. conducted COMSOL simulations. L.H., Y. Wang, C.S., and F.P. analyzed and discussed the data. All the authors contributed to the writing of the manuscript. **Competing interests:** The authors declare that they have no competing interests. **Data and materials availability:** All data needed to evaluate the conclusions in the paper are present in the paper and/or the Supplementary Materials.

Submitted 29 March 2022
Accepted 2 August 2022
Published 21 September 2022
10.1126/sciadv.abq2742